



# Polydopamine-mediated graphene oxide and nanohydroxyapatite-incorporated conductive scaffold with an immunomodulatory ability accelerates periodontal bone regeneration in diabetes

Yazhen Li<sup>a</sup>, Lu Yang<sup>b</sup>, Yue Hou<sup>b</sup>, Zhenzhen Zhang<sup>a</sup>, Miao Chen<sup>a</sup>, Maoxia Wang<sup>c</sup>, Jin Liu<sup>d</sup>, Jun Wang<sup>a,\*</sup>, Zhihe Zhao<sup>a,\*\*</sup>, Chaoming Xie<sup>b,\*\*\*</sup>, Xiong Lu<sup>b,\*\*\*\*</sup>

<sup>a</sup> State Key Laboratory of Oral Diseases, National Clinical Research Center for Oral Diseases, Department of Orthodontics, West China Hospital of Stomatology, Sichuan University, Chengdu, Sichuan, 610041, China

<sup>b</sup> Key Lab of Advanced Technologies of Materials, Ministry of Education, School of Materials Science and Engineering, Southwest Jiaotong University, Chengdu, Sichuan, 610031, China

<sup>c</sup> State Key Laboratory of Oral Diseases, National Clinical Research Center for Oral Diseases, Department of Oral Implantology, West China Hospital of Stomatology, Sichuan University, Chengdu, Sichuan, 610041, China

<sup>d</sup> Lab for Aging Research and National Clinical Research Center for Geriatrics, West China Hospital, Sichuan University, Chengdu, Sichuan, 610041, China

## ARTICLE INFO

### Keywords:

Polydopamine  
Graphene oxide  
Conductive scaffold  
ROS-Scavenging  
Macrophage polarization

## ABSTRACT

Regenerating periodontal bone tissues in the aggravated inflammatory periodontal microenvironment under diabetic conditions is a great challenge. Here, a polydopamine-mediated graphene oxide (PGO) and hydroxyapatite nanoparticle (PHA)-incorporated conductive alginate/gelatin (AG) scaffold is developed to accelerate periodontal bone regeneration by modulating the diabetic inflammatory microenvironment. PHA confers the scaffold with osteoinductivity and PGO provides a conductive pathway for the scaffold. The conductive scaffold promotes bone regeneration by transferring endogenous electrical signals to cells and activating Ca<sup>2+</sup> channels. Moreover, the scaffold with polydopamine-mediated nanomaterials has a reactive oxygen species (ROS)-scavenging ability and anti-inflammatory activity. It also exhibits an immunomodulatory ability that suppresses M1 macrophage polarization and activates M2 macrophages to secrete osteogenesis-related cytokines by mediating glycolytic and RhoA/ROCK pathways in macrophages. The scaffold induces excellent bone regeneration in periodontal bone defects of diabetic rats because of the synergistic effects of good conductive, ROS-scavenging, anti-inflammatory, and immunomodulatory abilities. This study provides fundamental insights into the synergistic effects of conductivity, osteoinductivity, and immunomodulatory abilities on bone regeneration and offers a novel strategy to design immunomodulatory biomaterials for treatment of immune-related diseases and tissue regeneration.

## 1. Introduction

Periodontitis is a common chronic and destructive inflammatory disease that leads to the destruction of periodontal tissue, including alveolar bone defects and gingival atrophy [1]. Aggravation of

periodontitis can eventually lead to loosening and loss of teeth and there is a link between periodontitis and systemic diseases that includes cardiovascular disease, gastrointestinal and colorectal cancers, diabetes, and insulin resistance [2]. The general strategies to reconstruct alveolar bone include debridement, guided bone/tissue regeneration

Peer review under responsibility of KeAi Communications Co., Ltd.

\* Corresponding author.

\*\* Corresponding author.

\*\*\* Corresponding author.

\*\*\*\* Corresponding author.

E-mail addresses: [wangjunv@scu.edu.cn](mailto:wangjunv@scu.edu.cn) (J. Wang), [zhzhao@scu.edu.cn](mailto:zhzhao@scu.edu.cn) (Z. Zhao), [xie@swjtu.edu.cn](mailto:xie@swjtu.edu.cn) (C. Xie), [luxiong\\_2004@163.com](mailto:luxiong_2004@163.com) (X. Lu).

<https://doi.org/10.1016/j.bioactmat.2022.03.021>

Received 3 December 2021; Received in revised form 22 February 2022; Accepted 12 March 2022

Available online 22 March 2022

2452-199X/© 2022 The Authors. Publishing services by Elsevier B.V. on behalf of KeAi Communications Co. Ltd. This is an open access article under the CC BY-NC-ND license (<http://creativecommons.org/licenses/by-nc-nd/4.0/>).

(GBR/GTR), and administration of antibiotics and bioactive molecules [3–5]. However, the clinical performance of these strategies is poor because of the rapid release of bioactive molecules and the limited innate bone regeneration capability in periodontitis [6]. Particularly, diabetes prolongs inflammation, also impairs bone coupling in periodontitis by over-activating osteoclasts that exacerbate bone resorption and decreasing the expression of growth factors that improve bone regeneration [7].

The immune system plays an important role in tissue regeneration [8,9]. In diabetes, both innate and adaptive immune responses are likely to contribute to the high level of inflammation and bone resorption [10]. A high level of glucose triggers the production of chemokines that activate immune cells. Long-term inflammatory conditions induce the generation of advanced glycation end products and ROS [11], which

results in overexpression of inflammatory cytokines in the local periodontal microenvironment. Moreover, diabetes is associated with prolonged polarization of M1 macrophages, which induces chronic inflammation, and reduction of M2 macrophages that promote tissue healing and exert anti-inflammatory effects [12,13]. Consequently, periodontal pathogenesis is worsened by the immune response in diabetes. Therefore, modulation of local immune responses is of great importance for periodontal bone regeneration in diabetes [14].

Recently, many efforts have been devoted to a GTR/GBR membrane for periodontal bone regeneration [4,15]. However, most of them are made from polytetrafluoroethylene and collagen, and therefore only act as physical barriers [16]. Although antibiotics and growth factors have been encapsulated in these membranes to promote periodontal bone regeneration, they may not be effective in the diabetic periodontal

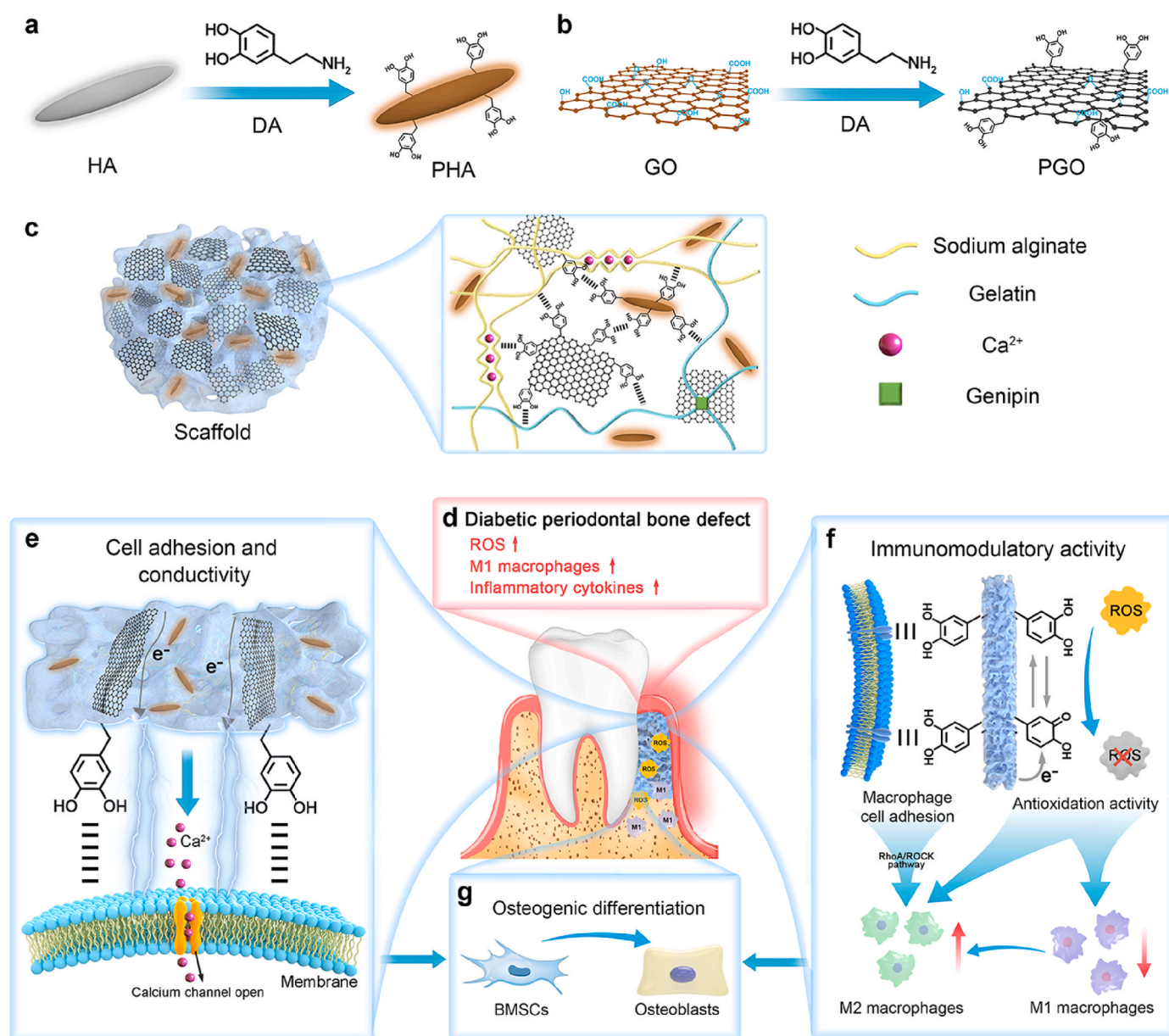


**Fig. 1.** Schematic illustration of the synthesis of the PGO-PHA-AG scaffold with multifunctional properties for potential application in periodontal bone regeneration in diabetes. (a) Schematic diagram of PHA synthesis. (b) Schematic diagram of PGO synthesis. (c) The scheme of interactions in physicochemical dual crosslinked PGO-PHA-AG scaffold network. (d) ROS, M1 macrophages, and inflammatory cytokines are overexpressed in the local diabetic periodontal microenvironment. (e) The scaffold promoted cell adhesion and transferred the endogenous electrical signals to cells, activating Ca<sup>2+</sup> channels. (f) The cell adhesion and ROS-scavenging properties of the PDA conferred the scaffold with an immunomodulatory activity that reduced M1 macrophage polarization and activated M2 macrophages that secreted osteogenesis-related cytokines. (g) The conductivity and immunomodulatory activity synergistically promoted periodontal bone regeneration.

microenvironment. Because of the disordered immunity of diabetes, biomaterials with the abilities to regenerate new bone and regulate immunity are required. Mussel-inspired polydopamine (PDA) is considered to be a promising antioxidant that reduces oxidative stress through scavenging ROS and down-regulating inflammatory mediators [17–19]. Our recent study showed that a PDA-based conductive silk fiber path accelerates diabetic wound healing by promoting cell adhesion, alleviating inflammation, relieving oxidative stress, and remodeling the extracellular matrix (ECM) [20]. Interestingly, the quality of diabetic wound healing was improved by conductive patch-induced bioelectricity transmission. Moreover, endogenous electrical signals promoted bone regeneration.

In this study, we developed a PDA-based conductive strategy to correct the hyperactive local immune response and improve the bone regeneration efficacy. A conductive alginate/gelatin (AG) scaffold was designed to modulate the diabetic inflammatory periodontal microenvironment and promote periodontal bone regeneration. Alginate is a linear polysaccharide, which is structurally similar to ECM, and has good biocompatibility [21,22]. Gelatin is a partial derivative of collagen containing the Arg-Gly-Asp (RGD) sequence, which is a major component of ECM [23]. The scaffold consisted of PDA-reduced graphene oxide (PGO) and PDA-modified hydroxyapatite nanoparticles (PHA). PHA and PGO were obtained by a one-step PDA functionalization strategy (Fig. 1a and b). Generally, GO has poor conductive ability [24]. Moreover, reduced GO (rGO) and HA exhibit unstable dispersibility in water [25,26]. PDA functionalization allowed the PHA and PGO to be well dispersed in an alginate and gelatin (AG) network to form an immunomodulatory scaffold for periodontal bone regeneration in diabetes (Fig. 1c and d). PGO shows better conductivity compared with GO because that it is partly reduced by PDA [24,27]. PGO in the scaffold provided a conductive pathway, which conferred the scaffold with conductivity. Via the conductivity, the scaffold transferred endogenous electrical signals to cells, which activated  $\text{Ca}^{2+}$  channels (Fig. 1e). Moreover, PDA functionalization endows the material with immunomodulatory activity [28]. The cell adhesion and ROS-scavenging properties of the PDA synergistically endowed the scaffold with an immunomodulatory activity that reduced M1 macrophage polarization to downregulate inflammatory cytokines, and activated M2 macrophages to secrete osteogenesis-related cytokines (Fig. 1f). The conductivity and immunomodulatory activity synergistically promoted alveolar bone regeneration in the diabetic inflammatory periodontal microenvironment (Fig. 1g).

## 2. Experimental section

### 2.1. Fabrication of the PGO-PHA-AG scaffold

First, 0.15 g of gelatin and 0.3 g of sodium alginate were added to 10 mL of deionized water. The solution was stirred for 3 h at 60 °C until the gelatin and sodium alginate powders were completely dissolved. 0.2 g of PHA and 0.1 g of PGO were then added to the mixture. Subsequently, genipin (0.02 g) was added to the mixed solution to cross-link the gelatin. The mixed solution was then injected into a mold, freeze-dried, and soaked in a  $\text{CaCl}_2$  solution (0.2 M) for 2 h to cross-link the sodium alginate. Finally, the scaffold was obtained by freeze-drying (−60 °C, 48 h). For comparison, we prepared AG scaffolds and PHA-AG scaffolds using the same assembly processes. The detailed contents are listed in Table S1. Details on the preparation of HA, PHA, GO, PGO, rGO and the characterization of scaffolds are provided in the Supporting Information.

### 2.2. Cell morphologies

Bone marrow mesenchymal stem cells (BMSCs) were extracted from one-week-old Sprague–Dawley (SD) rats. BMSCs ( $2 \times 10^4$  cells per well) were cultured on AG, PHA-AG, and PGO-PHA-AG scaffolds (2 mm in height, 10 mm in diameter) in 48-well plates for 24 h. Then, the cells

were stained with mouse monoclonal anti-vinculin antibody (1:300, 66305-1-Ig, Proteintech, USA) and cyanine dye 3 (Cy3)-conjugated phalloidin (F-actin; 1:200, CA1610, Solarbio, China) for 12 h at 4 °C. Donkey anti-mouse antibody, Alexa Fluor 488 (1:300, 34106ES60, YEASEN, China) was used as the secondary antibody. Finally, the cell nuclei were labeled with 4,6-diamidino-2-phenylindole (DAPI; ab1041139, Abcam, USA). Images were captured using a confocal laser scanning microscope (CLSM; LSM880, Zeiss, Germany). The cell spreading area of BMSCs on the different samples was analyzed using the ImageJ software (National Institutes of Health, USA). The morphologies of BMSCs cultured on the different scaffolds were observed via scanning electron microscopy (SEM; Gemini 300, Zeiss, Germany) after 3 d. The cell viability was quantified using a 3-(4,5-dimethylthiazol-2-yl)-2,5-diphenyltetrazolium bromide (MTT) assay. Further details are provided in the Supporting Information.

### 2.3. High-throughput electrical stimulation of BMSCs

A home-made high-throughput electrical stimulation (ES) device was used to evaluate the behaviors of BMSCs on AG, PHA-AG, and PGO-PHA-AG scaffolds with different ES levels (0, 300, 600, and 900 mV) [29,30]. BMSCs ( $4 \times 10^4$  cells per well) were electrically stimulated for 30 min per day in 24-well plates on the scaffolds. The expressions of osteogenic gene markers collagen type I alpha 1 (*COL1A1*), Osterix (*Osx*), and alkaline phosphatase (*ALP*) were analyzed by reverse transcription quantitative polymerase chain reaction (RT-qPCR). The primers used for target genes are listed in Table S2. The ALP activity was measured using an ALP kit (A059-2-2, Nanjing JianCheng Bioengineering Institute, China). The total protein was measured using a bicinchoninic acid assay kit (A045-4-2, Nanjing JianCheng Bioengineering Institute, China). BMSCs ( $4 \times 10^4$  cells per well) were electrically stimulated for 30 min per day in 24-well plates under the scaffolds. The ALP staining was performed using a BCIP/NBT ALP color development kit (C3206, Beyotime, China) after 7 d of culturing with ES (300 mV) or without ES. Calcium deposition was determined by alizarin red S (ARS) staining (G3280, Solarbio, China) and quantitative analysis after 21 d of culturing with ES (300 mV) or without ES [31]. The images of ALP staining and ARS staining were captured using stereomicroscope (SMZ18, Nikon, Japan) and invert microscope (TI2-U, Nikon, Japan). Details on RT-qPCR and quantitative analysis of ARS staining are provided in the Supporting Information.

### 2.4. Intracellular calcium measurement

BMSCs were seeded on the PGO-PHA-AG scaffold at a density of  $5 \times 10^4$  cells per well in 24-well plates and cultured at 37 °C for seven days, followed by treatment for 30 min with ES (300 mV) or without ES per day. Cells were then washed with PBS three times and incubated with 2  $\mu\text{M}$  of Fluo-4 AM (500  $\mu\text{L}$  per well, S1060, Beyotime, China) for 30 min at 37 °C. Intracellular  $\text{Ca}^{2+}$  levels were measured using a flow analyzer (Cytoflex, Beckman, USA).

### 2.5. Cellular ROS scavenging activity

A reactive oxygen species assay kit (2',7'-dichloro fluorescein diacetate, DCFH-DA; S0033S, Beyotime, China) was used to test the cellular ROS scavenging activity. RAW 264.7 cells ( $3 \times 10^5$  cells per well) were cultured with AG, PHA-AG, or PGO-PHA-AG scaffolds in 24-well plates for 12 h. The ROS levels were measured using CLSM (LSM880, Zeiss, Germany) and flow analyzer (Cytoflex, Beckman, USA). Further details are provided in the Supporting Information.

### 2.6. Polarization of macrophages

RAW 264.7 was polarized into M1 phenotypes by treatment with 100 ng/mL LPS (L4391, Sigma, USA) and cultured with different

scaffolds. For inducible nitric oxide synthase (iNOS) and CD163 staining, RAW 264.7 cultured with different scaffolds were incubated with primary antibodies, including rabbit polyclonal anti-iNOS antibody (1:200, ab3523, Abcam, USA) and rabbit monoclonal anti-CD163 antibody (1:200, ab182422, Abcam, USA) respectively after 24 h of culturing. Donkey anti-rabbit antibody, Alexa Fluor 488 (1:800, A-21206, Invitrogen, USA) and donkey anti-rabbit antibody, Alexa Fluor 555 (1:800, A-31572, Invitrogen, USA) were used as secondary antibodies. The cell nuclei were labeled with DAPI. Images were captured using CLSM (FV3000, Olympus, Japan). All the images were transformed to 8-bit binary images, and the fluorescence intensity was calculated by normalized analysis. The proteins, iNOS and CD163, were tested by Western blot (WB). iNOS (1:1000, ab3523, Abcam, USA), CD163 (1:500, ab182422, Abcam, USA), and  $\beta$ -ACTIN (1:5000, 66009-1-Ig, Proteintech, USA) were utilized as primary antibodies. HRP-conjugated goat anti-rabbit antibody (1:5000, A0208, Beyotime, China) and HRP-conjugated goat anti-mouse antibody (1:5000, A0216, Beyotime, China) were utilized as secondary antibodies. WB images were captured using the ChemiDoc Touch Imaging System (Bio-rad, California, USA). For flow cytometry, the cells were incubated with antibodies against CD86 (159203, Biolegend, USA) and CD206 (141707, Biolegend, USA). The expressions of genes, including interleukin-1 $\beta$  (*IL-1 $\beta$* ), iNOS, tumor necrosis factor- $\alpha$  (*TNF- $\alpha$* ), *CD206*, *CD163*, arginase 1 (*Arg1*), bone morphogenetic protein-2 (*BMP-2*), and transforming growth factor- $\beta$ 1 (*TGF- $\beta$ 1*) were analyzed by RT-qPCR. To investigate the effects of macrophages (cultured on various scaffolds) on osteogenesis, macrophages were cultured with different scaffolds for 1 d. Then, the macrophage conditioned medium was collected. Afterwards, BMSCs were cultured in medium that made up of collected macrophage conditioned medium on different scaffolds, and Rat Mesenchymal Stem Cell Osteogenic Differentiation Medium (RAXMX-90021, Cyagen Biosciences Inc., China) at a ratio of 1:2 [32]. The procedures of ALP staining, ALP activity and ARS staining as former. The images of ALP staining and ARS staining were captured using stereomicroscope (SMZ18, Nikon, Japan) and invert microscope (TI2-U, Nikon, Japan). The expressions of osteogenic gene markers, including *ALP*, *COL1A1*, and runt-related transcription factor 2 (*Runx2*), were analyzed by RT-qPCR. The primers used for target genes are listed in Table S2 and further details are provided in the Supporting Information.

### 2.7. Transcriptome sequencing and data analysis

Macrophages were cultured with AG, PHA-AG, and PGO-PHA-AG scaffolds for 24 h. The macrophages were then treated with TRIzol reagent (Invitrogen, USA) and stored at  $-80^{\circ}\text{C}$  before sequencing. RNA sequencing was performed using Illumina HiSeq X10 (Illumina, USA). The data were normalized using the fragments per kilobase per million reads method. Gene ontology and KEGG pathway enrichment analyses were performed using the free online Majorbio Cloud Platform ([www.majorbio.com](http://www.majorbio.com)). The transcriptome analysis was further verified by RT-qPCR and WB. The procedures of the RT-qPCR and WB as former. The expressions of genes, including hypoxia inducible factor-1 $\alpha$  (*HIF-1 $\alpha$* ), pyruvate dehydrogenase kinase 1 (*Pdk1*), phosphoglycerate kinase 1 (*Pgk1*), cell division cycle 42 (*Cdc42*), Rac family small GTPase 1 (*Rac1*), and Rho-associated coiled-coil containing protein kinase (*ROCK*), were analyzed by RT-qPCR. The primers used for target genes are listed in Table S2. *HIF-1 $\alpha$*  (1:2000, 20960-1-AP, Proteintech, USA), *Pdk1* (1:500, 18262-1-AP, Proteintech, USA), *Pgk1* (1:500, 17811-1-AP, Proteintech, USA), *Cdc42* (1:1000, DF6322, Affinity Biosciences, China), *Rac1* (1:1000, AF9178, Affinity Biosciences, China), *MLC* (1:1000, DF7911, Affinity Biosciences, China), *p-MLC* (1:1000, AF8618, Affinity Biosciences, China), and  $\beta$ -ACTIN (1:5000, 66009-1-Ig, Proteintech, USA) were utilized as primary antibodies. HRP-conjugated goat anti-rabbit antibody (1:5000, A0208, Beyotime, China) and HRP-conjugated goat anti-mouse antibody (1:5000, A0216, Beyotime, China) were utilized as secondary antibodies. WB images were captured using the ChemiDoc

Touch Imaging System (Bio-rad, California, USA).

### 2.8. In-vivo study

Thirty-two SD rats (male; 200–220 g; age: 8 weeks) were intraperitoneally injected with 65 mg/kg streptozocin (STZ; Sigma, USA) to establish a diabetic model [31]. A standard defect size of  $3 \times 2 \times 1 \text{ mm}^3$  was created for periodontitis of the rat mandible [33]. AG, PHA-AG, and PGO-PHA-AG scaffolds ( $\Phi 3 \times 2 \times 1 \text{ mm}^3$ ) were implanted into SD rats to evaluate the osteoinductivity in vivo. The rats were euthanized 14 and 28 d later. The samples were fixed for histology, immunofluorescence, and micro-CT assays. All animal experiments were performed according to protocols approved by the Research Ethics Committee of West China Hospital of Stomatology (WCHSIRB-D-2021-544). Further details are provided in the Supporting Information.

### 2.9. Statistical analysis

All results were analyzed by a one-way analysis of variance (ANOVA) with a Tukey's post hoc test. The data are expressed as mean  $\pm$  standard deviation with  $n \geq 3$ . \* $P < 0.05$  and \*\* $P < 0.01$  were considered statistically significant.

## 3. Results and discussion

### 3.1. Characterization of the PGO-PHA-AG scaffold

PDA successfully reduced GO owing to its redox activity, and stabilizing and binding abilities (Fig. S1). The PGO had a typical transparent and wrinkled thin sheet structure [34], and the size of PGO was approximately 600 nm (Fig. 2a). After PDA functionalization, the PGO exhibited more stable dispersibility in water compared with hydriodic acid-reduced GO (rGO) (Fig. 2b). PDA was also used to functionalize various nanohydroxyapatites (PHA) (Fig. S2). TEM imaging showed that the length of rod-shaped PHA was approximately 50 nm (Fig. 2c). Moreover, PDA modification did not affect the structures of GO and HA (Fig. S3). High resolution TEM (HRTEM) imaging revealed that the lattice spacing of PHA NP was  $3.4 \text{ \AA}$  (Fig. 2d), which corresponded to the (0 0 2) crystallographic plane of HA [35,36]. XRD patterns revealed that PHA had the same crystal structure as HA (Fig. S2c), which implied that PDA functionalization did not affect the structural integrity or crystallinity of the HA. Moreover, the PHA had good water dispersibility and were easily incorporated into the AG scaffold after PDA functionalization. PHA showed the typical Tyndall effect in water, whereas the HA nanoparticles scattered light (Fig. 2e).

The PGO and PHA-incorporated AG scaffold (PGO-PHA-AG) had the uniform porous structure of the scaffold and typical wrinkled structure of PGO (Fig. 2f and g). Moreover, the PGO-PHA-AG scaffold had denser microstructures than the scaffold without PGO and PHA (Fig. S4). EDS mapping analysis showed Ca and P in the PGO-PHA-AG scaffold, which demonstrated that PHA was incorporated uniformly (Fig. 2h). PGO conferring the scaffold with good electrical conductivity. As shown in Fig. 2i, a light-emitting diode (LED) was illuminated in a PGO-PHA-AG scaffold-connected circuit. The conductivity of the scaffold increased with PGO content (Fig. 2j). The maximum conductivity was  $1.6 \text{ S/cm}$  with 10 wt % PGO in the scaffold. Thus, the PGO-PHA-AG scaffold with a PGO content of 10 wt % was used in subsequent experiments. Furthermore, the scaffold maintained good conductivity during the deformation (Fig. 2k).

The PGO-PHA-AG scaffold had good mechanical properties owing to the nano-reinforcement effect of the PGO and PHA. The compressive strength of the PHA-AG scaffold was increased from about 30 to 50 kPa with the addition of PHA and the compressive strength of the PGO-PHA-AG scaffold was increased from about 50 to 140 kPa with the increase in PGO content from 0 to 10 wt % (Fig. 2l and Fig. S5). A significant increase in the compressive modulus from 12 kPa to 50 kPa was detected

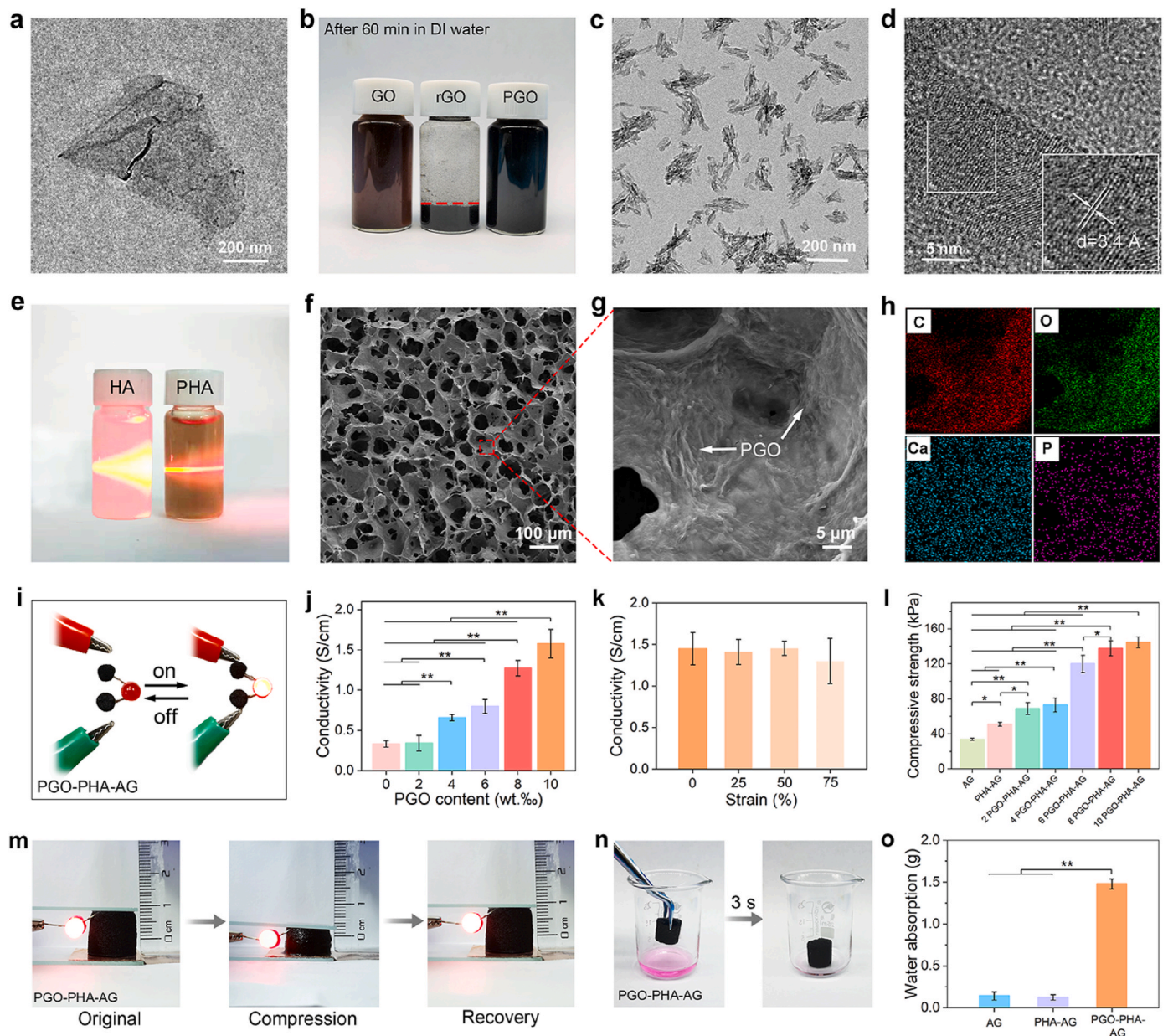


**Fig. 2.** Characterization of the PGO, PHA, and PGO-PHA-AG scaffold. (a) TEM image of PGO. (b) Digital images of GO, reduced GO (rGO), and PGO dispersed in deionized (DI) water after 60 min. (c) TEM and (d) HRTEM images of PHA. (e) PHA exhibited the Tyndall effect in DI water. (f, g) SEM micrographs of the PGO-PHA-AG scaffold (10 wt % PGO). (h) EDS elemental mapping images of the PGO-PHA-AG scaffold (10 wt % PGO). (i) A light-emitting diode (LED) was illuminated in a PGO-PHA-AG scaffold (10 wt % PGO)-connected circuit. (j) Conductivities of scaffolds with different contents of PGO. (k) Conductivity of the PGO-PHA-AG scaffold after compression. (l) Compressive strength of AG, PHA-AG, and PGO-PHA-AG scaffolds (2, 4, 6, 8, 10 wt % PGO). (m) The PGO-PHA-AG scaffold (10 wt % PGO) with an illuminated LED was compressed and recovered. (n) Digital images of the PGO-PHA-AG scaffold (10 wt % PGO) placed in DI water containing rhodamine for 3 s. (o) Water absorption capacity of AG, PHA-AG, and PGO-PHA-AG scaffold (10 wt % PGO).

with the addition of PHA and PGO (Fig. S6). The scaffold recovered to its initial state after compression, and maintained its good conductivity (Fig. 2m). The good mechanical properties were attributed to the catechol groups on the surface of PGO, which interacted with the scaffold network and increased the crosslinking density [27]. Although the shape of the scaffold was unmodifiable after cross-link, the “pentacle”, “heart”, “bone”, and “triangle” shapes like scaffolds were prepared because of good elasticity and cutability of the PGO-PHA-AG scaffold (Fig. S7). Thus, the shapes of the scaffolds can be cut according to the clinical requirements. The PGO-PHA-AG scaffold exhibited a good liquid absorption capacity. The scaffold rapidly absorbed water within 3 s (Fig. 2n). Moreover, the water absorption capacity of the PGO-PHA-AG scaffold was higher than that of AG and PHA-AG scaffolds (Fig. 2o and

Fig. S8). This was conducive to the infiltration of tissue fluid and nutrient exchange at the implantation site. Moreover, the PGO-PHA-AG scaffold was biodegradable, making it suitable for long-term implantation (Fig. S9).

### 3.2. Cell adhesion and high throughput electrical stimulation

The PGO-PHA-AG scaffold also exhibited good cytocompatibility to support cell adhesion and proliferation. To explore the adhesion and spreading of bone marrow mesenchymal stem cells (BMSCs) on the surface of the scaffold, we stained BMSCs with 4',6-diamidino-2-phenylindole (nucleus), cyanine dye 3 (Cy3)-conjugated phalloidin (F-actin), and a mouse monoclonal anti-vinculin antibody and observed

their morphologies at day 1. As shown in Fig. 3a and b, BMSCs spread better on PGO-PHA-AG than on bare AG and PHA-AG scaffolds because of the cell affinity of the catechol group and wrinkled structure of PGO [27]. As shown in Fig. S10, SEM images showed that BMSCs spread better on the surface of PGO-PHA-AG scaffold after 3 days culture. An MTT assay showed that cell proliferation on the PGO-PHA-AG scaffold was higher than that on AG and PHA-AG scaffolds after 3 d and all the scaffolds showed good cytocompatibility (Fig. 3c).

Thanks to the conductivity and cell affinity of the scaffold, the cells adhered to the scaffold and responded to the external ES. Thus, the PGO-PHA-AG scaffold acted as a conductive platform to regulate cell behaviors by transferring electrical signals. The synergistic effects of the scaffold components and electrical signals were investigated using a home-designed high throughput ES device (Fig. 3d). Without ES, the ALP activity of BMSCs on the PHA-AG scaffold was higher than that of the AG scaffold because of the osteoinductivity of HA. With an ES

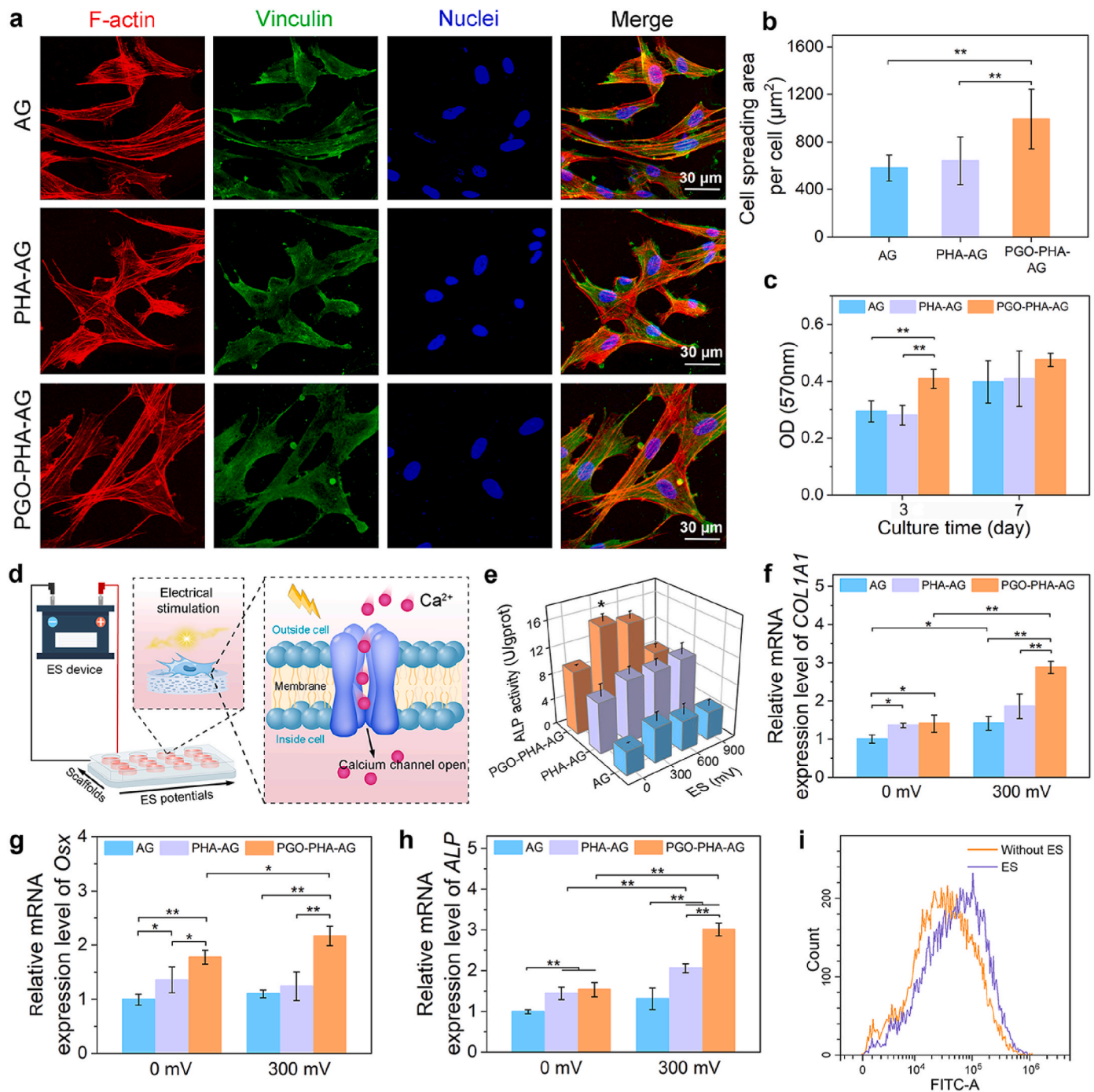


**Fig. 3.** Cell adhesion and high throughput electrical stimulation (ES) of BMSCs on the surfaces of scaffolds. (a) Cell morphologies of BMSCs on the surfaces of AG, PHA-AG, and PGO-PHA-AG scaffolds (10 wt % PGO). (b) Cell spreading area of BMSCs. (c) Proliferation of BMSCs on the various scaffolds after 3 and 7 d of culturing. (d) Schematic of the high throughput ES. The conductive scaffold delivered electrical signals to BMSCs, which resulted in a  $Ca^{2+}$  influx. Then, intracellular signaling cascades were activated, which contributed to the up-regulation of genes related to osteogenesis and eventually promoted the osteogenesis of BMSCs. (e) Alkaline phosphatase (ALP) activity of BMSCs on AG, PHA-AG, and PGO-PHA-AG scaffolds (10 wt % PGO) under various ES potentials after 14 d. (f–h) Osteogenesis-related gene expressions of collagen type I alpha 1 (*COL1A1*), Osterix (*Osx*), and *ALP* with or without ES after 14 d. (i) Flow cytometry of Fluo-4 AM-labeled cells in the fluorescein isothiocyanate (FITC)-A channel, indicating intracellular  $Ca^{2+}$  concentration of cells on the PGO-PHA-AG scaffold (10 wt % PGO) with or without ES.

voltage of 300 mV, the PGO-PHA-AG scaffold induced the largest degree of ALP expression (Fig. 3e).

Gene expression analysis confirmed the positive synergistic effect of electrical signals and chemical cues from the scaffold on osteogenic differentiation of BMSCs (Fig. 3f–h). Expressions of *COL1A1*, *Osx*, and *ALP* in BMSCs on the PHA-AG scaffold was significantly higher than that

on the AG scaffold, which indicated that PHA promoted osteogenic differentiation. Using ES, the expression of osteogenic genes in cells on the PGO-PHA-AG scaffold was significantly higher than that without ES, which revealed that the electrical signals further improved the differentiation of BMSCs into osteoblasts. The color of ALP staining showed a similar trend with the gene expression, which exhibited the highest ALP

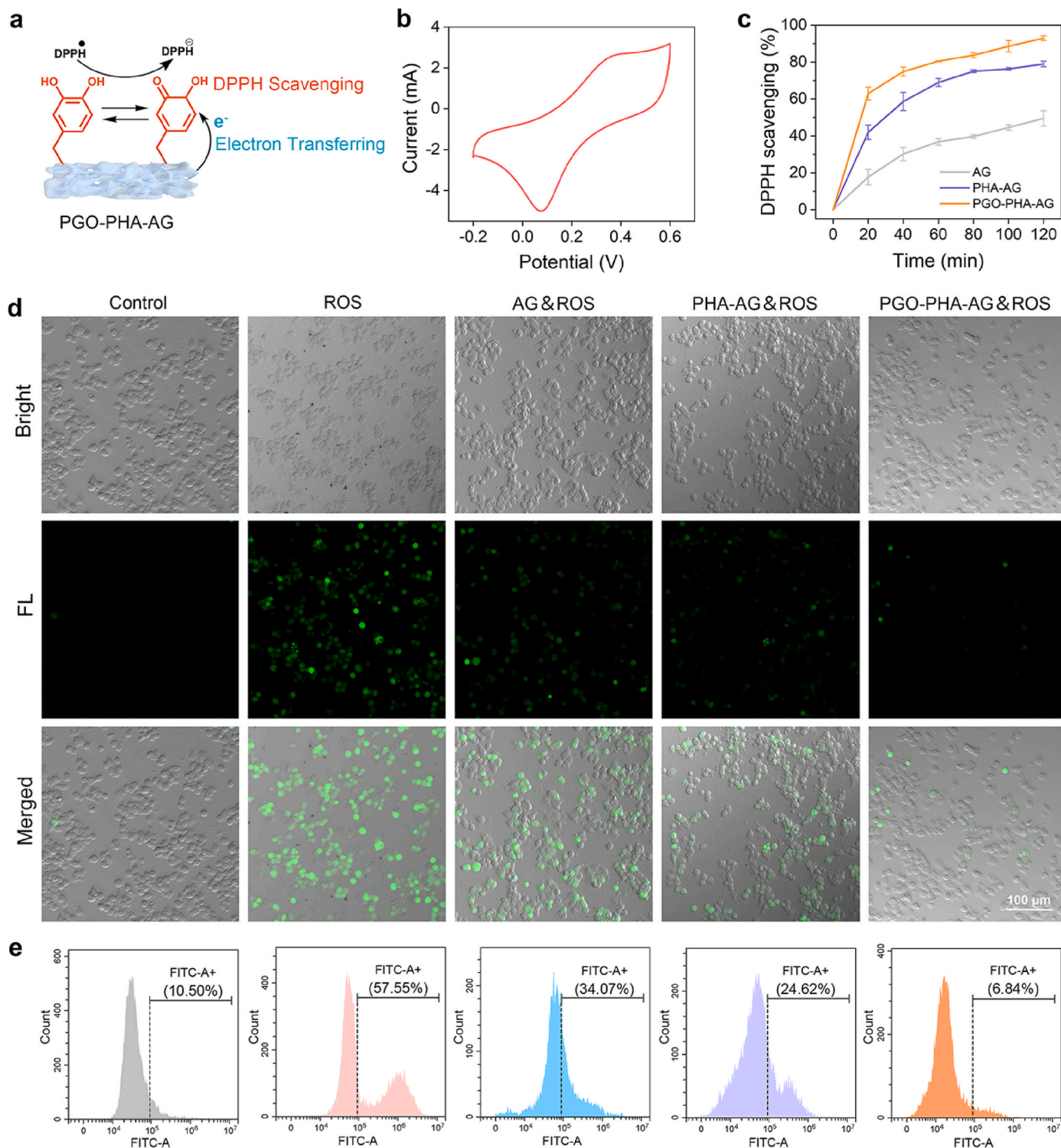


**Fig. 4.** Antioxidative property of the PGO-PHA-AG scaffold (10 wt % PGO) in vitro. (a) Antioxidative mechanism of the PGO-PHA-AG scaffold. (b) Cyclic voltammetry curve of the PGO-PHA-AG scaffold. (c) DPPH-scavenging efficiency of AG, PHA-AG, and PGO-PHA-AG scaffolds. (d) Intracellular ROS-scavenging performance of AG, PHA-AG, and PGO-PHA-AG scaffolds. (e) Flow cytometric analysis of 2',7'-dichloro fluorescein diacetate (DCFH-DA)-labeled cells in the FITC-A channel on the various scaffolds. Bars on the right span the stained ROS-presenting subpopulations and the percentage is shown.

activity in the PGO-PHA-AG group under ES (Fig. S11a and b). Moreover, the ARS staining demonstrated that only small mineralized nodules were observed in the AG group, but more mineralized nodules were observed in the PGO-PHA-AG group under ES (Fig. S11c–e).

These results demonstrated that the PGO-PHA-AG scaffold is a promising platform for osteogenic differentiation. The osteoinductive PHA and conductive PGO in the scaffold synergistically enhanced the differentiation of BMSCs into osteoblasts. The ES improved osteogenic differentiation of BMSCs on the conductive PGO-PHA-AG scaffold because the electrical signals can stimulate L-type voltage-gated  $\text{Ca}^{2+}$  channels in the cell membrane, leading to the increase of intracellular  $\text{Ca}^{2+}$  [37]. To prove this mechanism, the intracellular  $\text{Ca}^{2+}$  concentration of BMSCs with ES or without ES was evaluated by Fluo-4 AM. As shown in Fig. 3i, there was a significant difference in the intracellular  $\text{Ca}^{2+}$  concentrations between the two groups. Intracellular  $\text{Ca}^{2+}$  increased significantly with ES.

The mechanism of the scaffold on its regulatory effects on BMSCs can be summarized to three aspects. First, the cell-affinity of PDA promoted the cell adhesion and spreading on the scaffold, which might enhance osteogenic differentiation of BMSCs by activating cytoskeletal tension via RhoA/ROCK signaling pathways [38,39]. Second, PHA is osteoinductive, which has ability to promote osteogenic differentiation of BMSCs [25]. Third, The ES could stimulate L-type voltage-gated  $\text{Ca}^{2+}$  channels in the cell membrane, leading to the increase of intracellular  $\text{Ca}^{2+}$ . Moreover, the ES could induce the electrically mediated stress in the cells (electroporation), resulting in the increase of intracellular  $\text{Ca}^{2+}$  [40], which also contribute to osteogenic differentiation of BMSCs on the conductive PGO-PHA-AG scaffold.

### 3.3. Antioxidative properties

The PGO-PHA-AG scaffold exhibited excellent antioxidative property because of the catechol groups on the PHA and PGO. A high level of ROS is one of the main causes of periodontal inflammation, especially under diabetic conditions, which severely hinder tissue regeneration [41]. ROS were eliminated by catechol groups, and catechol groups were converted to quinone groups. Additionally, PGO facilitated electron transfer to quinone groups, which reduced the quinone groups to catechol groups (Fig. 4a). The dynamic catechol/quinone redox system gave the scaffold a high ROS-scavenging property. The redox reaction in the PGO-PHA-AG scaffold was evaluated by Cyclic Voltammetry (CV) scanning (Fig. 4b). The CV curve showed a pair of redox peaks at 0.38 and 0.08 V, which corresponded to the transition of catechol groups to quinone groups and the reverse reaction, respectively.

A 1,1-diphenyl-2-picrylhydrazyl (DPPH) free radical scavenging assay was used to evaluate the antioxidative activities of the scaffolds. UV–vis spectra showed that the DPPH peak in the PGO-PHA-AG scaffold was the lowest, which demonstrated that the PGO-PHA-AG scaffold had the highest DPPH-scavenging activity (Fig. S12). The DPPH-scavenging efficiency of the scaffolds was calculated after reacting in the dark for 20, 40, 60, 80, 100, and 120 min. The results showed that the DPPH-scavenging ratios of AG, PHA-AG, and PGO-PHA-AG scaffolds increased over time (Fig. 4c). However, without catechol groups, the DPPH-scavenging ratio of the AG scaffold only reached 49% in 120 min. In contrast, the PGO-PHA-AG scaffold had a maximum DPPH-scavenging ratio of 93% in 120 min.

The excellent antioxidative property of the PGO-PHA-AG scaffold protected cells from ROS-induced damage. To demonstrate the cellular ROS-scavenging property of the PGO-PHA-AG scaffold, a DCFH-DA probe was applied to investigate the intracellular ROS level in RAW 264.7 cells after culturing with various scaffolds (Fig. 4d). The PGO-PHA-AG scaffold exhibited the lowest fluorescence intensity. The results of flow cytometry showed that the ROS positivity of the AG scaffold was 34.07% (Fig. 4e). In sharp contrast, the ROS positivity was reduced to 6.84% in the PGO-PHA-AG scaffold. These results demonstrated the effectiveness of the PGO-PHA-AG scaffold to prevent cell damage from

excessive amounts of ROS under oxidative stress.

### 3.4. Immunomodulatory activity of the PGO-PHA-AG scaffold

The PGO-PHA-AG scaffold modulated macrophage polarization from M1 to M2 and promoted M2 macrophages to secrete osteogenesis-related cytokines. Macrophages affect inflammatory and tissue healing processes via two distinct polarization states: M1 macrophages that induce chronic inflammation and M2 macrophages that promote tissue healing and anti-inflammation [42,43]. However, M1 macrophages do not polarize to the M2 phenotype under a diabetic condition [33]. To explore the influence of the PGO-PHA-AG scaffold on macrophages, RAW 264.7 macrophages were seeded on various scaffolds. iNOS (a marker of M1 macrophage activation) and CD163 (a marker of M2 macrophage polarization) were selected for immunofluorescence staining [44]. As shown in Fig. 5a and Fig. S13, the immunofluorescence staining results showed that the level of iNOS in the PGO-PHA-AG group was significantly lower than that in the AG and PHA-AG groups. In contrast, the level of CD163 in the PGO-PHA-AG group was highest in all groups. Moreover, the results of WB also showed the same trend (Fig. 5b). To further confirm the phenotypes of polarized macrophages on the various scaffolds, CD86 (a marker of M1 macrophages) and CD206 (a marker of M2 macrophages)-positive cells were selected to evaluate macrophage polarization by flow cytometric analysis. As shown in Fig. 5c, the proportion of M2 macrophages on various scaffolds showed the following trend: PGO-PHA-AG (44.29%) > PHA-AG (19.14%) > AG (13.56%). The proportion of M1 macrophages on scaffolds showed the following trend: PGO-PHA-AG (14.13%) < PHA-AG (24.81%) < AG (42.59%). Moreover, PGO-PHA-AG induced lower expression levels of M1-related genes (*IL-1 $\beta$* , *TNF- $\alpha$* , and *iNOS*), but higher expression of M2-related genes (*CD206*, *CD163*, and *Arg1*) in comparison with AG and PHA-AG groups (Fig. 5d and e). These results indicated that the PGO-PHA-AG scaffold significantly induced M2 macrophage polarization and reduced M1 macrophage polarization compared with PHA-AG and AG scaffolds.

In addition to regulating inflammatory environments, M2 macrophages mediate bone regeneration by secreting osteogenesis-related factors [45]. *BMP-2* and *TGF- $\beta$ 1* were chosen as osteogenic gene markers to evaluate the activation of M2 macrophages by the scaffolds. The PGO-PHA-AG scaffold induced higher expression levels of *BMP-2* and *TGF- $\beta$ 1* than PHA-AG and AG scaffolds (Fig. 5f). Moreover, the effect of macrophages regulated by scaffolds on BMSCs were also evaluated. First, macrophages were cultured with different scaffolds for 1 d. Then, the macrophage conditioned medium was collected. The osteogenic differentiation of BMSCs cultured with macrophage conditioned medium was evaluated by ALP staining, ALP activity, ARS staining and osteogenic gene expression. After incubation for 7 d, the color of ALP staining of BMSCs in the PGO-PHA-AG medium group was darker than that in the AG and PHA-AG groups (Fig. 5g). PGO-PHA-AG medium group exhibited highest ALP activity (Fig. 5h). Moreover, expression levels of the osteogenic gene markers, including *ALP*, *COL1A1*, and *Runx2*, were up-regulated in cells cultured with PHA-AG versus AG medium groups, and the expression levels were further up-regulated in cells cultured with PGO-PHA-AG medium group (Fig. 5i). After incubation for 14 d, obvious mineralized nodules were observed in the PGO-PHA-AG medium group (Fig. 5j and k). Thus, these results suggested that excellent effect of macrophage regulation by the PGO-PHA-AG scaffold on osteogenic differentiation of BMSCs. This favorable effect can be attributed to the immunomodulatory ability of the PGO-PHA-AG scaffold which promoted M2 macrophages to secrete osteogenesis-related cytokines.

### 3.5. Immunomodulatory mechanism

To elucidate the immunomodulatory mechanism of the PGO-PHA-AG scaffold, we performed transcriptome analyses of RAW 264.7 cells

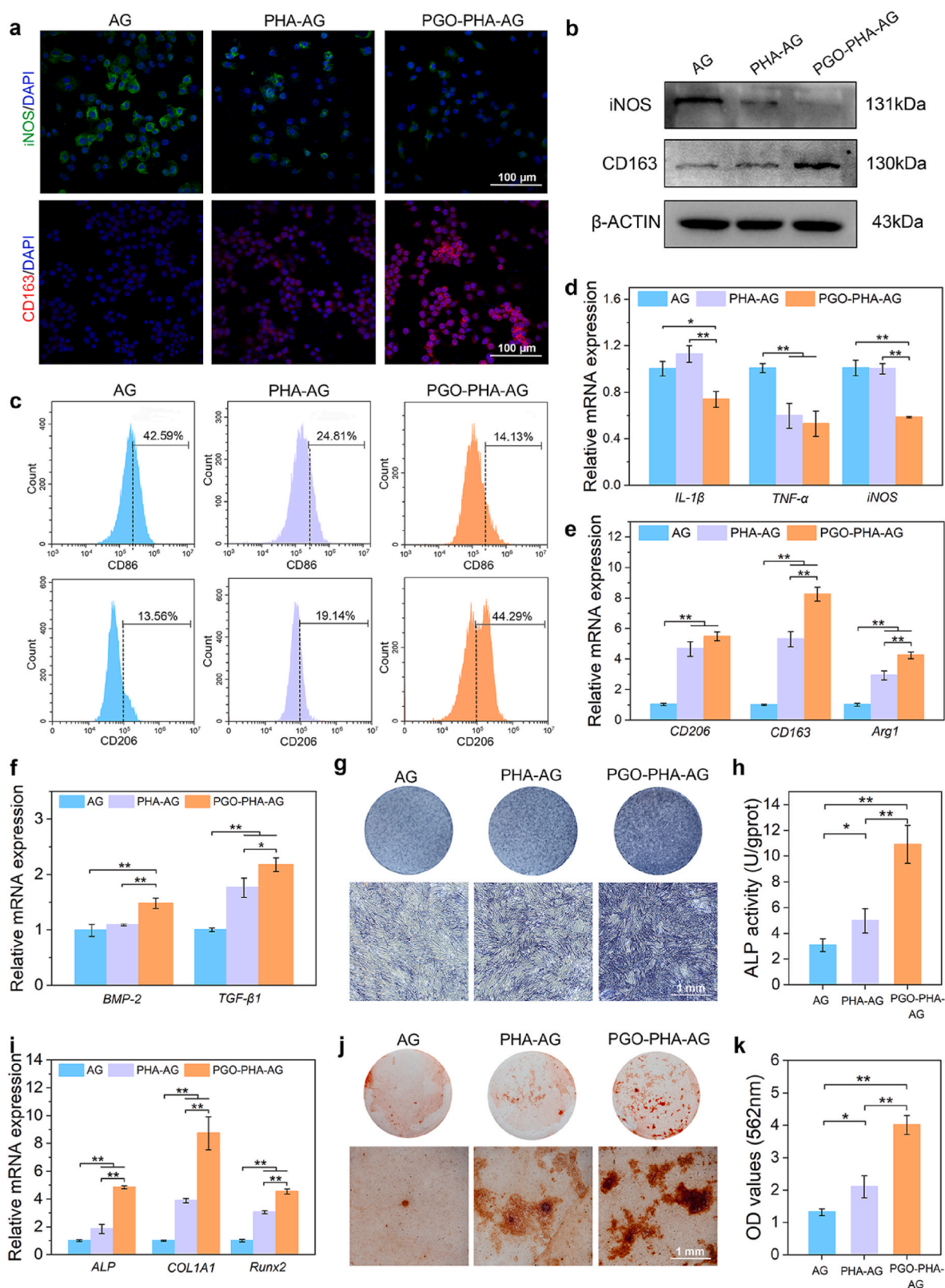


**Fig. 5.** Immunomodulatory property of the PGO-PHA-AG scaffold (10 wt % PGO) of macrophages in vitro. (a) Fluorescence microscopy of inducible nitric oxide synthase (iNOS), CD163, and nuclear staining of macrophages cultured with different scaffolds. (b) Western blot (WB) analysis of iNOS and CD163. (c) Polarization of macrophages was evaluated by expression of CD86 (M1) and CD206 (M2) using flow cytometry. (d) Relative mRNA expression of M1 macrophage-related genes interleukin-1 $\beta$  (*IL-1 $\beta$* ), tumor necrosis factor- $\alpha$  (*TNF- $\alpha$* ), and iNOS. (e) Relative mRNA expression of M2 macrophage-related genes *CD206*, *CD163*, and arginase 1 (*Arg1*). (f) Relative mRNA expression of osteogenic gene markers, bone morphogenetic protein-2 (*BMP-2*) and transforming growth factor- $\beta$ 1 (*TGF- $\beta$ 1*) secreted by macrophages. (g, h) ALP staining and ALP activity quantitative analyses of BMSCs after 7 d cultured with macrophage conditioned medium. (i) Osteogenesis-related gene expressions of *ALP*, *COL1A1*, and runt-related transcription factor 2 (*Runx2*) secreted by BMSCs after 7 d cultured with macrophage conditioned medium. (j, k) Alizarin red S (ARS) staining and quantitative analysis of ARS staining of BMSCs after 14 d cultured with macrophage conditioned medium.

cultured on various scaffolds. The results revealed a large number of different genes by comparing different samples (1128 genes in AG versus PHA-AG, 1097 genes in PHA-AG versus PGO-PHA-AG, and 2465 genes in AG versus PGO-PHA-AG) and they shared 108 genes (Fig. S14). The volcano plots showed 215 up-regulated and 913 down-regulated genes (AG versus PHA-AG), 568 up-regulated and 529 down-regulated genes (PHA-AG versus PGO-PHA-AG), and 1667 up-regulated and 798 down-regulated genes (AG versus PGO-PHA-AG), which revealed large differences in gene expression (Fig. S15). On the basis of these differently expressed genes, we performed gene ontology enrichment analysis on three gene ontology categories: biological processes (BP), cellular components (CC), and molecular functions (MF) (Fig. 6a). The 20 most enriched terms between AG and PGO-PHA-AG included the immune response, microtubule-based movement in biological processes, myosin complexes, microtubule binding, microtubule motor activity, motor activity, and actin filament binding in molecular functions, which correlated with the polarization of macrophages.

To further evaluate the underlying signal transduction pathways, we performed Kyoto Encyclopedia of Genes and Genomes (KEGG) pathway enrichment. Generally, glycolysis is heightened in LPS-treated

macrophages by HIF-1-dependent transcriptional activation [46]. LPS induces transportation of citrate outside the mitochondria by increasing expression of the citrate carrier. Metabolization of citrate generates NADPH, which is catalyzed by NADPH oxidase to produce ROS [47]. ROS induce *HIF-1α* mRNA accumulation and HIF-1α protein synthesis, and thus promote glycolysis. Heightened glycolysis promotes M1 macrophage polarization and the secretion of proinflammatory cytokines [48]. In this study, the ROS in macrophages were effectively scavenged in the PGO-PHA-AG group. Thus, the HIF-1 signaling pathway was significantly down-regulated in KEGG analysis (Fig. 6b). The M1 macrophage activation-related TNF signaling pathway was also down-regulated [49]. Moreover, transcriptome analysis revealed down-regulation of *HIF-1α* and glycolytic pathway-related genes, namely, *Pdk1*, *Pgk1*, glucokinase (*Gck*) and proinflammatory cytokines, namely, interleukin-6 (*IL-6*) and *iNOS* (Fig. 6c). The gene expression analysis suggested that *HIF-1α*, *Pdk1*, and *Pgk1* in the PGO-PHA-AG group were significantly down-regulated as compared with others (Fig. S16a), indicating that the glycolytic pathway had been inhibited by the PGO-PHA-AG scaffold (Fig. 6d). WB analysis showed a similar trend (Fig. S16c).

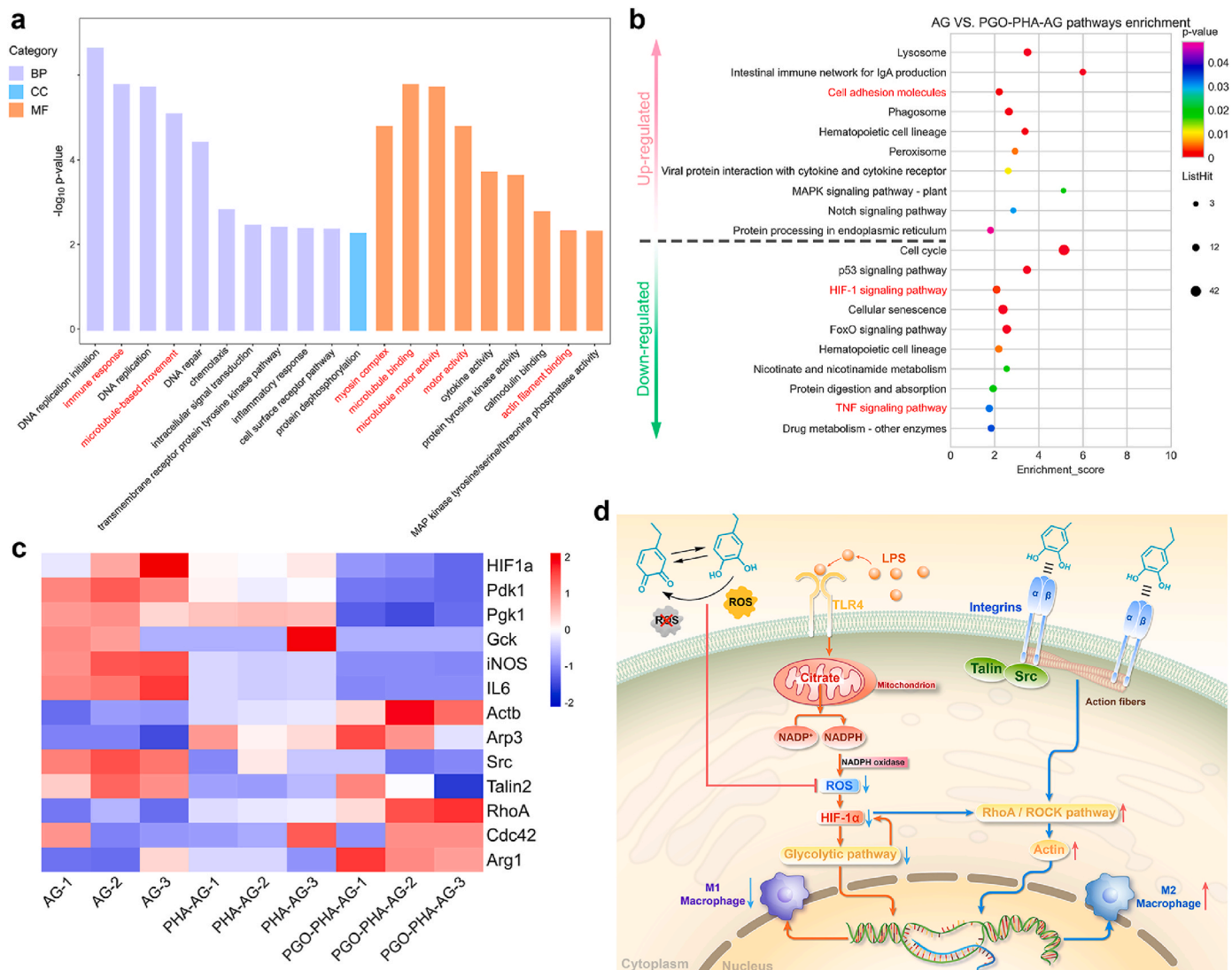


**Fig. 6.** Mechanistic analysis of macrophage polarization induced by the PGO-PHA-AG scaffold (10 wt % PGO). (a) Gene ontology analysis of all genes in macrophages cultured on AG versus PGO-PHA-AG scaffolds. BP, biological processes; CC, cellular components; MF, molecular functions. (b) Enriched KEGG pathways of AG versus PGO-PHA-AG. (c) Heatmap analysis of differentially expressed genes involved in the HIF-1 signaling pathway, the glycolytic pathway, proinflammatory cytokines, cell adhesion molecules, cytoskeleton arrangement, and mechanotransduction. (d) Schematic illustration of the mechanism of macrophage polarization induced by the PGO-PHA-AG scaffold.

Furthermore, the cell adhesion molecule pathway was up-regulated, which is related to M2 macrophage activation [45]. This result suggested that the cell adhesion of PDA may promote M2 macrophage polarization. PDA facilitated the extension of cell protrusions such as lamellipodia and filopodia [50]. Filopodia sense and respond to extracellular cues by transducing biochemical signals to modulate gene expression, which activates macrophages. Filopodia are linked to cell motility and migration, and are required for several processes involving macrophages that occur during immunity and inflammatory processes against infection [51]. This is consistent with the results of the gene ontology enrichment analysis (Fig. 6a). PDA promoted the interaction between macrophages and the ECM through integrins, which play a crucial role in cell adhesion, macrophage activation, and podosome formation [50,52]. For macrophages, podosomes have been reported to dominate cell–matrix interactions, which have a similar role to focal adhesions [53]. Transcriptome analysis revealed that the PGO-PHA-AG scaffold up-regulated marker genes of podosome formation, namely actin (*Actb*) and actin-related protein 3 (*Arp3*), indicating that the PGO-PHA-AG scaffold facilitated podosome formation (Fig. 6c). Conversely, the integrin-binding protein-related genes, *Src* and *taln2*, were down-regulated by the PGO-PHA-AG scaffold, promoting podosome formation [51]. Downstream of podosome formation is the Rho family of guanosine triphosphatases, which has been reported to be involved in actin stress fibers (*RhoA*), filipodia (*Cdc42*) and lamellipodia (*Rac1*) [54,55]. *RhoA* and *Cdc42* were up-regulated by the PGO-PHA-AG scaffold. Gene expressions including *Cdc42*, *Rac1*, and *ROCK*, were up-regulated by the PGO-PHA-AG scaffold (Fig. S16b). WB analysis suggested that the expressions of *Cdc42*, *Rac1*, and a specific phosphorylated ROCK substrate [phosphorylated myosin light chain (p-MLC)] in the PGO-PHA-AG group were significantly up-regulated as compared with others (Fig. S16c), indicating that the RhoA/ROCK signaling pathway had been activated by the PGO-PHA-AG scaffold. Moreover, *Arg1*, a marker of M2 macrophage activation, was up-regulated. The researchers have confirmed that the RhoA/ROCK signaling pathway played a key role in M2 macrophage activation [45, 56], which agrees with our results. These results indicated that the PGO-PHA-AG scaffold activated M2 macrophage polarization via the RhoA/ROCK signaling pathway (Fig. 6d). Additionally, ROS scavenging inhibited RhoA/ROCK signaling pathway [57], which was an underlying signaling pathway of the PGO-PHA-AG scaffold to activate M2 macrophage polarization.

### 3.6. PGO-PHA-AG scaffold promotes periodontal bone regeneration in diabetic rats

A type I diabetic rat mandibular periodontal fenestration model was chosen to evaluate the regulatory effect of the scaffolds on periodontal bone regeneration under diabetic conditions (Fig. 7a). Micro-CT analysis showed that the bone mineral density (BMD) of the PGO-PHA-AG group were higher than those of other groups at 28 d post-surgery (Fig. 7b and c). The ratio of the bone volume to total volume (BV/TV) of the PGO-PHA-AG and PHA-AG scaffold group were higher than the blank and AG groups (Fig. 7d). Hematoxylin–eosin (H&E) staining showed that the defect areas in the blank and AG scaffold groups were filled with fibrous tissue (Fig. 7e), which indicated that such a region could not self-repair under diabetic conditions. Conversely, half of the defect region in the PHA-AG group was filled with new bone. The defect region in the PGO-PHA-AG group was almost filled with new bone. Histomorphometric analysis was performed to evaluate new bone and mature bone formation. Analysis of H&E stained sections demonstrated that new bone was higher in the PGO-PHA-AG group than that in the Blank, AG, and PHA-AG groups (Fig. S17a). Masson's trichrome staining was used to further observe the repair of new bone tissue in the different groups. Masson's trichrome staining showed that the mature bone in the PGO-PHA-AG group was more than that in the AG and PHA-AG scaffold groups, which confirmed that the PGO-PHA-AG scaffold promotes the

maturation of new bone (Fig. 7f and Fig. S17b).

Numerous studies on diabetes-associated bone regeneration have ignored the vital fact that diabetes mellitus is a chronic inflammatory disease and the long-term inflammatory environment induces the generation of advanced glycation end products and excessive ROS, which in turn aggravate local inflammation [58]. The critical roles of ROS scavenging and inflammation control under diabetic conditions have been neglected, which has led to difficulty in the regeneration of periodontal defects. Removal of excessive ROS in the affected area, protection of cells from excessive ROS, and inflammation control are crucial to repair periodontal bone defects. Thus, the effect of the antioxidative scaffold on oxidative stress was evaluated. As shown in Fig. 7g–j, immunofluorescence and quantitative analysis of 8-hydroxy-2'-deoxyguanosine (8-OHdG) and 4-hydroxynonenal (4-HNE), typical biomarkers of oxidative stress, showed that their expression was decreased significantly in the PGO-PHA-AG group at 14 d after implantation. Moreover, expression of inflammatory cytokine IL-6 was examined. As shown in Fig. 7k and l, expression of IL-6 was the highest in the blank group, indicating inflammation. Conversely, a significant reduction in expression of IL-6 was observed in the PGO-PHA-AG group because of its anti-inflammatory activity.

To further investigate the in vivo immunomodulatory activity of the PGO-PHA-AG scaffold, iNOS and CD206 fluorescence staining was performed to identify the phenotype of macrophages in periodontal bone defects at 14 days after implantation. Expression of iNOS in the PGO-PHA-AG group was lower than that in other groups, indicating the small number of M1 macrophages in the defect region (Fig. 8a and b). Additionally, expression of CD206 in the PGO-PHA-AG group was higher than that in the other three groups, revealing the presence of a large number of M2 macrophages in the defect region (Fig. 8c and d). Furthermore, osteogenic differentiation-related factors, osteocalcin (OCN) and Runx2, were highly expressed in the PGO-PHA-AG scaffold group, which indicated mineralization of the bone extracellular matrix (Fig. 8e–h).

Although BV/TV in the PGO-PHA-AG group showed no significance to that in the PHA-AG group, the quality of the bone in PGO-PHA-AG was higher than that of PHA-AG. First, BMD in the PGO-PHA-AG group was significantly higher than that in the PHA-AG (Fig. 7c). Second, Masson's trichrome staining showed that the mature bone in the defect area in the PGO-PHA-AG group was more than that in the AG and PHA-AG groups (Fig. 7f and Fig. S17b). The higher quality was attributed to addition of PGO, which have indicated by the immunofluorescence staining. After adding PGO, the in vivo inflammatory and oxidative stress markers were down-regulated (Fig. 7g–l and 8a–d), whereas the osteogenic differentiation-related factors were up-regulated (Fig. 8e–h). Thus, PGO promoted the quality of the bone regeneration. All these results showed that the PGO-PHA-AG scaffold was an effective immunomodulatory material for periodontal bone repair under diabetic conditions.

The immunomodulatory activity of PGO-PHA-AG in bone regeneration was attributed to the following reasons. First, PGO and PHA conferred cell affinity to the scaffold, thereby enhancing the adhesion and proliferation abilities of cells on the scaffold. Second, PGO conferred the scaffold with good conductivity. The conductive scaffold responded to an endogenous electric field to stimulate  $Ca^{2+}$  ion channels on the cell membrane. At this time,  $Ca^{2+}$  released from the PGO-PHA-AG scaffold flowed into the cell and activated osteogenesis-related pathways, which ultimately led to osteogenic differentiation of cells and periodontal bone regeneration. Third, the scaffold had an excellent ROS-scavenging ability that reduced oxidative stress in the defect region. Fourth, the scaffold controlled the local inflammation by reducing M1 macrophages and down-regulating proinflammatory cytokines. Fifth, M2 macrophages were activated to secrete osteogenesis-related cytokines. These factors synergistically contributed to immunomodulating the inflammatory microenvironment and promoting periodontal bone regeneration under diabetic conditions.

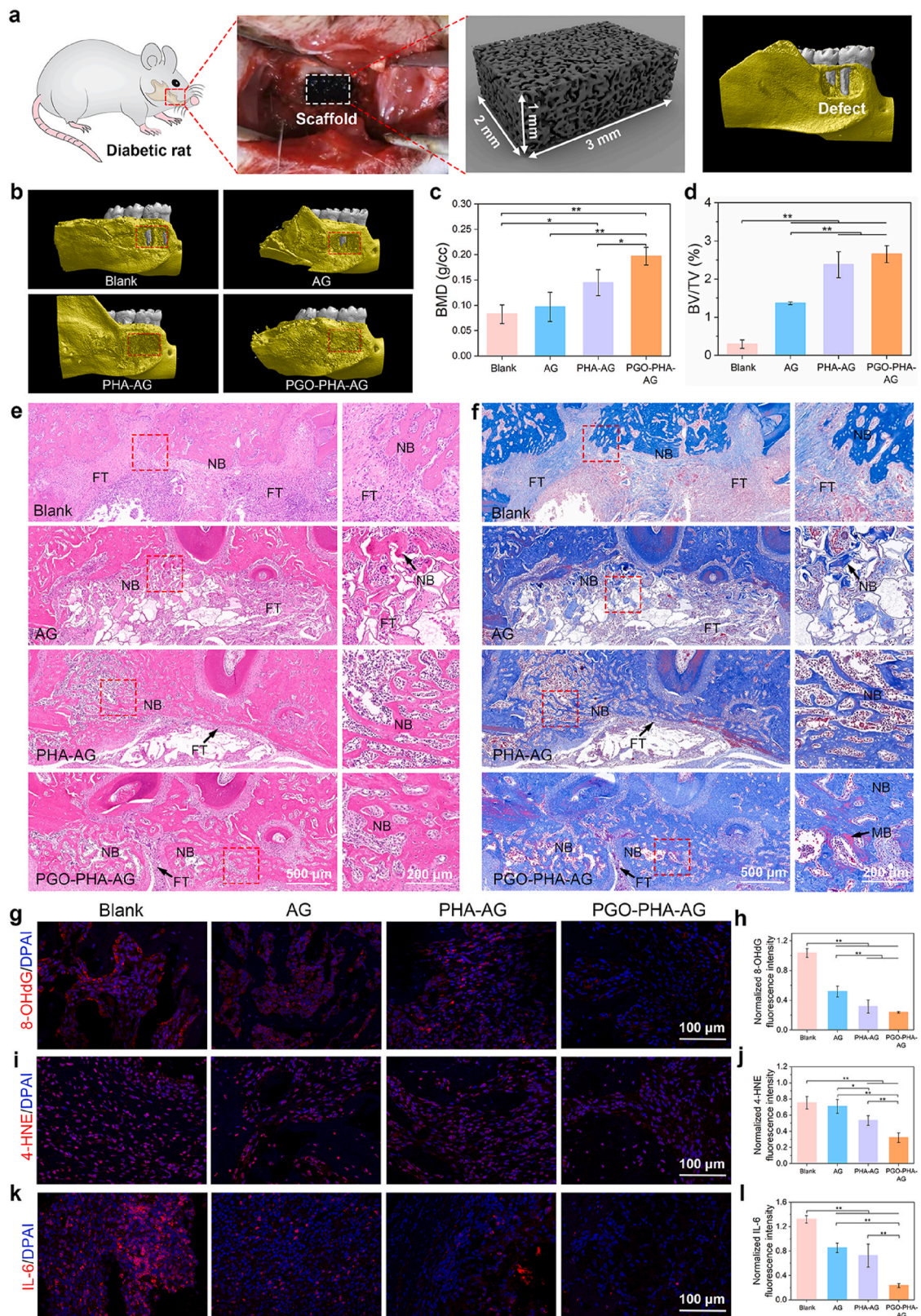


**Fig. 7.** In vivo periodontal bone regeneration in diabetic condition. (a) Surgical operation for scaffold implantation into a periodontal defect model in diabetic rats. (b) Micro-CT images of the rat mandible at the site of implantation. (c) Bone mineral density (BMD) in the four groups. (d) Ratio of the bone volume to total volume (BV/TV) in the four groups. (e, f) H&E and Masson's trichrome staining of the defect area at 28 days after implantation. FT, fibrous tissue; NB, new bone; MB, mature bone. (g–l) Immunofluorescence staining of 8-hydroxy-2'-deoxyguanosine (8-OHdG), 4-hydroxynonenal (4-HNE), and interleukin-6 (IL-6) (red) in defect areas and normalized fluorescence intensity.

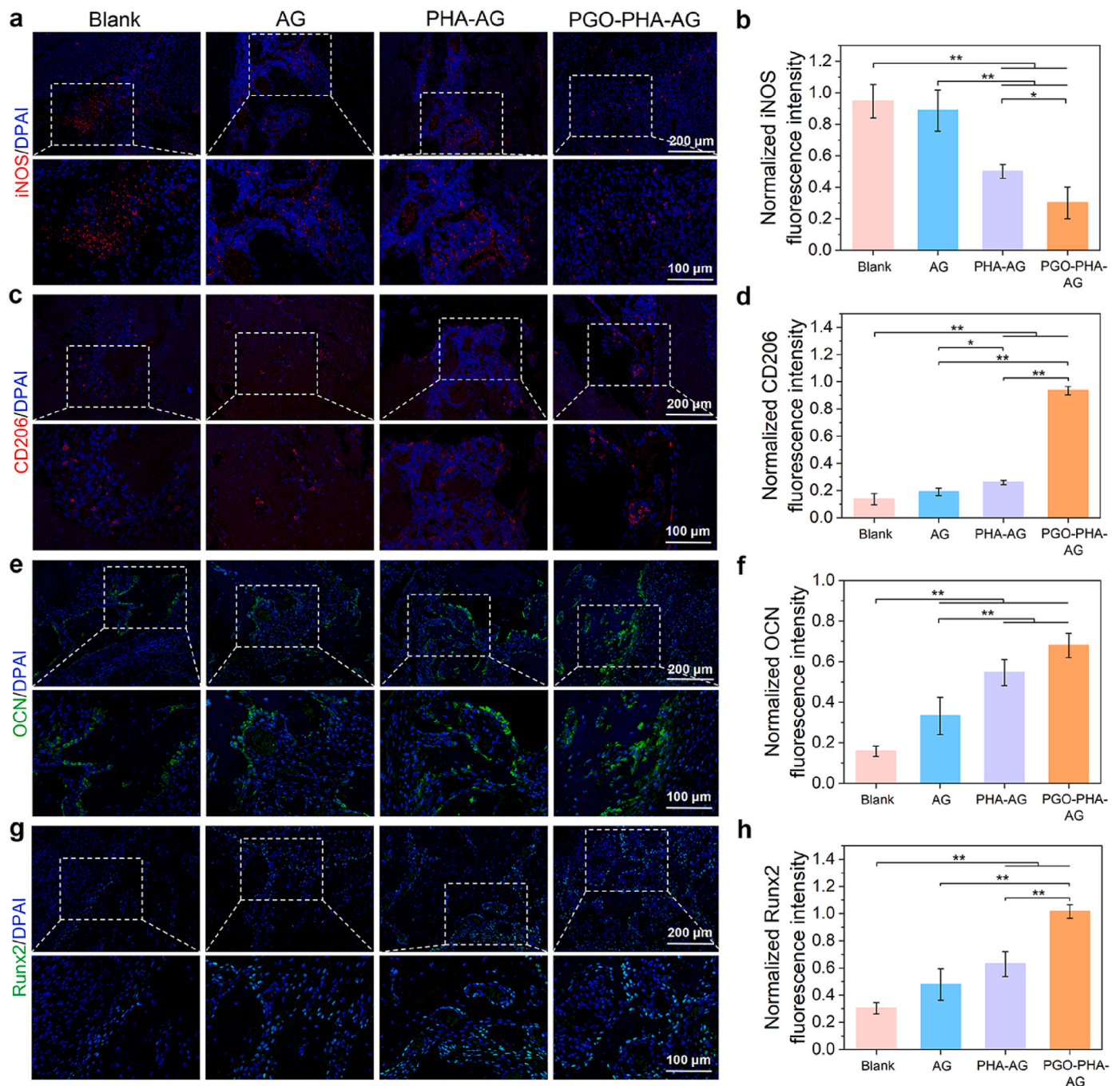


**Fig. 8.** Immunofluorescence staining of defect areas. (a–d) Immunofluorescence staining of iNOS and CD206 (red) in defect areas, and normalized fluorescence intensity. (e–h) Immunofluorescence staining of osteocalcin (OCN) and Runx2 (green) in defect areas, and normalized fluorescence intensity.

#### 4. Conclusion

A conductive, ROS-scavenging, anti-inflammatory, immunomodulatory scaffold was developed to enhance periodontal bone regeneration. The scaffold was achieved by incorporating PHA and PGO into a physiochemical dual crosslinked AG network. The scaffold exhibited several advantages in diabetic periodontal bone regeneration. First, PDA modification allowed PGO to be uniformly dispersed in the scaffold, which provided well-connected conductive pathways. Second, catechol groups on PDA facilitated cell adhesion on the scaffold. Third, with the PGO-provided conductive pathways, electrical signals were easily transferred to cells, which activated  $Ca^{2+}$  channels and promoted  $Ca^{2+}$  influx. Fourth, catechol groups conferred the scaffold with effective

ROS-scavenging and anti-inflammatory activities. Fifth, the scaffold also suppressed M1 macrophage polarization and activated M2 macrophages to secrete osteogenesis-related cytokines. The scaffold accelerated periodontal bone healing in the aggravated periodontal inflammatory microenvironment under diabetic conditions because of the synergistic effects of conductive, ROS-scavenging, anti-inflammatory, and immunomodulatory abilities.

#### CRediT authorship contribution statement

**Yazhen Li:** Conceptualization, Methodology, Data curation, Formal analysis, Writing – original draft, Validation. **Lu Yang:** Methodology, Validation. **Yue Hou:** Formal analysis, Validation, Software. **Zhenzhen**

**Zhang:** Methodology, Data curation, Validation. **Miao Chen:** Methodology, Validation. **Maoxia Wang:** Validation, Software. **Jin Liu:** Data curation, Formal analysis. **Jun Wang:** Conceptualization, Funding acquisition, Project administration. **Zhihe Zhao:** Conceptualization, Funding acquisition, Project administration, Writing – review & editing. **Chaoming Xie:** Conceptualization, Funding acquisition, Project administration, Writing – review & editing. **Xiong Lu:** Conceptualization, Funding acquisition, Project administration, Writing – review & editing.

## Declaration of competing interest

The authors declare that they have no known competing financial interests or personal relationships that could have appeared to influence the work reported in this paper.

## Acknowledgements

This work was supported by grants from Sichuan Key Research and Development Program of China (22ZDYF2034), National Natural Science Foundation of China (grant no. 82072071, 82072073), Key-Area Research and Development Program of Guang Dong Province (2019B010941002), Shenzhen Funds of the Central Government to Guide Local Scientific and Technological Development (2021SZVUP123), Sichuan Science and Technology Program (2020YFS0170), Fundamental Research Funds for the Central Universities (2682020ZT79), Guangdong Basic and Applied Basic Research Foundation (2021B1515120019), and Research and Develop Program, West China Hospital of Stomatology Sichuan University (RD-03-202012, RD-03-202101).

## Appendix A. Supplementary data

Supplementary data to this article can be found online at <https://doi.org/10.1016/j.bioactmat.2022.03.021>.

## References

- [1] F.S.C. Szczepanik, M.L. Grossi, M. Casati, M. Goldberg, M. Glogauer, N. Fine, H. C. Tenenbaum, Periodontitis is an inflammatory disease of oxidative stress: we should treat it that way, *Periodontol* 84 (1) (2020) 45–68, 2000.
- [2] E.M. Cardoso, C. Reis, M.C. Manzaneres-Céspedes, Chronic periodontitis, inflammatory cytokines, and interrelationship with other chronic diseases, *Postgrad. Med.* 130 (1) (2018) 98–104.
- [3] Z. Sheikh, J. Qureshi, A.M. Alshahrani, H. Nassar, Y. Ikeda, M. Glogauer, B. Ganss, Collagen based barrier membranes for periodontal guided bone regeneration applications, *Odontology* 105 (1) (2017) 1–12.
- [4] D. Abdelaziz, A. Hefnawy, E. Al-Wakeel, A. El-Fallal, I.M. El-Sherbiny, New biodegradable nanoparticles-in-nanofibers based membranes for guided periodontal tissue and bone regeneration with enhanced antibacterial activity, *J. Adv. Res.* 28 (2021) 51–62.
- [5] J. Tan, M. Zhang, Z. Hai, C. Wu, J. Lin, W. Kuang, H. Tang, Y. Huang, X. Chen, G. Liang, Sustained release of two bioactive factors from supramolecular hydrogel promotes periodontal bone regeneration, *ACS Nano* 13 (5) (2019) 5616–5622.
- [6] F.M. Chen, J. Zhang, M. Zhang, Y. An, F. Chen, Z.F. Wu, A review on endogenous regenerative technology in periodontal regenerative medicine, *Biomaterials* 31 (31) (2010) 7892–7927.
- [7] S. Pacios, J. Kang, J. Galicia, K. Gluck, H. Patel, A. Ovyadi-Mandel, S. Petrov, F. Alawi, D.T. Graves, Diabetes aggravates periodontitis by limiting repair through enhanced inflammation, *Faseb. J.* 26 (4) (2012) 1423–1430.
- [8] Z. Julier, A.J. Park, P.S. Briquez, M.M. Martino, Promoting tissue regeneration by modulating the immune system, *Acta Biomater* 53 (2017) 13–28.
- [9] A.B. Aurora, E.N. Olson, Immune modulation of stem cells and regeneration, *Cell Stem Cell* 15 (1) (2014) 14–25.
- [10] P.M. Preshaw, A.L. Alba, D. Herrera, S. Jepsen, A. Konstantinidis, K. Makrilakis, R. Taylor, Periodontitis and diabetes: a two-way relationship, *Diabetologia* 55 (1) (2012) 21–31.
- [11] K. Byun, Y. Yoo, M. Son, J. Lee, G.B. Jeong, Y.M. Park, G.H. Salekdeh, B. Lee, Advanced glycation end-products produced systemically and by macrophages: a common contributor to inflammation and degenerative diseases, *Pharmacol. Ther.* 177 (2017) 44–55.
- [12] S.M. Huang, C.S. Wu, M.H. Chiu, C.H. Wu, Y.T. Chang, G.S. Chen, C.E. Lan, High glucose environment induces M1 macrophage polarization that impairs keratinocyte migration via TNF-alpha: an important mechanism to delay the diabetic wound healing, *J. Dermatol. Sci.* 96 (3) (2019) 159–167.
- [13] E.C. Leal, E. Carvalho, A. Tellechea, A. Kafanas, F. Tecilzich, C. Kearney, S. Kuchibhotla, M.E. Auster, E. Kokkottou, D.J. Mooney, F.W. LoGerfo, L. Pradhan-Nabzdyk, A. Veves, Substance P promotes wound healing in diabetes by modulating inflammation and macrophage phenotype, *Am. J. Pathol.* 185 (6) (2015) 1638–1648.
- [14] D.T. Graves, Z. Ding, Y. Yang, The impact of diabetes on periodontal diseases, *Periodontol* 82 (1) (2020) 214–224, 2000.
- [15] L. Lei, Y. Yu, J. Han, D. Shi, W. Sun, D. Zhang, L. Chen, Quantification of growth factors in advanced platelet-rich fibrin and concentrated growth factors and their clinical efficacy as adjunctive to the GTR procedure in periodontal intrabony defects, *J. Periodontol.* 91 (4) (2020) 462–472.
- [16] T. Zhou, X. Liu, B. Sui, C. Liu, X. Mo, J. Sun, Development of fish collagen/bioactive glass/chitosan composite nanofibers as a GTR/GBR membrane for inducing periodontal tissue regeneration, *Biomed. Materials* 12 (5) (2017), 055004.
- [17] H.A. Lee, Y. Ma, F. Zhou, S. Hong, H. Lee, Material-independent surface chemistry beyond polydopamine coating, *Acc. Chem. Res.* 52 (3) (2019) 704–713.
- [18] Z. Yang, X. Zhao, R. Hao, Q. Tu, X. Tian, Y. Xiao, K. Xiong, M. Wang, Y. Feng, N. Huang, G. Pan, Bioclickable and mussel adhesive peptide mimics for engineering vascular stent surfaces, *Proc. Natl. Acad. Sci. U.S.A.* 117 (28) (2020) 16127–16137.
- [19] X. Wang, X. Sun, D. Gan, M. Soubrier, H.-Y. Chiang, L. Yan, Y. Li, J. Li, S. Yu, Y. Xia, Bioadhesive and conductive hydrogel-integrated brain-machine interfaces for conformal and immune-evasive contact with brain tissue, *Matter* 5 (2022) 1–20.
- [20] Z. Jia, J. Gong, Y. Zeng, J. Ran, J. Liu, K. Wang, C. Xie, X. Lu, J. Wang, Bioinspired conductive silk microfiber integrated bioelectronic for diagnosis and wound healing in diabetes, *Adv. Funct. Mater.* 31 (19) (2021).
- [21] U. Schloßmacher, H.C. Schröder, X. Wang, Q. Feng, B. Diehl-Seifert, S. Neumann, A. Trautwein, W.E.G. Müller, Alginate/silica composite hydrogel as a potential morphogenetically active scaffold for three-dimensional tissue engineering, *RSC Adv* 3 (28) (2013) 11185–11194.
- [22] Y. Yi, C. Xie, J. Liu, Y. Zheng, J. Wang, X. Lu, Self-adhesive hydrogels for tissue engineering, *J. Mater. Chem. B* 9 (42) (2021) 8739–8767.
- [23] C.-H. Chang, H.-C. Liu, C.-C. Lin, C.-H. Chou, F.-H. Lin, Gelatin–chondroitin–hyaluronan tri-copolymer scaffold for cartilage tissue engineering, *Biomaterials* 24 (26) (2003) 4853–4858.
- [24] L. Han, X. Lu, M. Wang, D. Gan, W. Deng, K. Wang, L. Fang, K. Liu, C.W. Chan, Y. Tang, L.T. Weng, H. Yuan, A mussel-inspired conductive, self-adhesive, and self-healable tough hydrogel as cell stimulators and implantable bioelectronics, *Small* 13 (2) (2017).
- [25] Y. Jiang, X. Pan, M. Yao, L. Han, X. Zhang, Z. Jia, J. Weng, W. Chen, L. Fang, X. Wang, Y. Zhang, R. Duan, F. Ren, K. Wang, X. Chen, X. Lu, Bioinspired adhesive and tumor microenvironment responsive nanoMOFs assembled 3D-printed scaffold for anti-tumor therapy and bone regeneration, *Nano Today* 39 (2021).
- [26] P.H.M. Gohari, M.H. Nazarpak, M. Solati-Hashjin, The effect of adding reduced graphene oxide to electrospun polycaprolactone scaffolds on MG-63 cells activity, *Mater. Today Commun.* 27 (2021) 102287.
- [27] P. Tang, L. Han, P. Li, Z. Jia, K. Wang, H. Zhang, H. Tan, T. Guo, X. Lu, Mussel-inspired electroactive and antioxidant scaffolds with incorporation of polydopamine-reduced graphene oxide for enhancing skin wound healing, *ACS Appl. Mater. Interfaces* 11 (8) (2019) 7703–7714.
- [28] J. Wang, J. Lin, L. Chen, L. Deng, W. Cui, Endogenous electric fields-coupled electrospun short fiber via collecting wound exudation, *Adv. Mater.* (2021) 2108325.
- [29] C. Xie, P. Li, L. Han, Z. Wang, T. Zhou, W. Deng, K. Wang, X. Lu, Electroresponsive and cell-affinitive polydopamine/polypyrrole composite microcapsules with a dual-function of on-demand drug delivery and cell stimulation for electrical therapy, *NPG Asia Mater* 9 (3) (2017) e358–e358.
- [30] L. Yan, T. Zhou, L. Han, M. Zhu, Z. Cheng, D. Li, F. Ren, K. Wang, X. Lu, Conductive cellulose bio-nanosheets assembled biostable hydrogel for reliable bioelectronics, *Adv. Funct. Mater.* 31 (17) (2021).
- [31] M. Chen, D. Jing, R. Ye, J. Yi, Z. Zhao, PPARbeta/delta accelerates bone regeneration in diabetic mellitus by enhancing AMPK/mTOR pathway-mediated autophagy, *Stem Cell Res. Ther.* 12 (1) (2021) 566.
- [32] X. Dai, B.C. Heng, Y. Bai, F. You, X. Sun, Y. Li, Z. Tang, M. Xu, X. Zhang, X. Deng, Restoration of electrical microenvironment enhances bone regeneration under diabetic conditions by modulating macrophage polarization, *Bioact. Mater.* 6 (7) (2021) 2029–2038.
- [33] Z. Hu, C. Ma, X. Rong, S. Zou, X. Liu, Immunomodulatory ECM-like microspheres for accelerated bone regeneration in diabetes mellitus, *ACS Appl. Mater. Interfaces* 10 (3) (2018) 2377–2390.
- [34] C. Xie, H. Sun, K. Wang, W. Zheng, X. Lu, F. Ren, Graphene oxide nanolayers as nanoparticle anchors on biomaterial surfaces with nanostructures and charge balance for bone regeneration, *J. Biomed. Mater. Res.* 105 (5) (2017) 1311–1323.
- [35] X. Fan, B. Feng, Z. Liu, J. Tan, W. Zhi, X. Lu, J. Wang, J. Weng, Fabrication of TiO2 nanotubes on porous titanium scaffold and biocompatibility evaluation in vitro and in vivo, *J. Biomed. Mater. Res.* 100 (12) (2012) 3422–3427.
- [36] X. Lu, Y.B. Wang, Y.R. Liu, J.X. Wang, S.X. Qu, W. Jie, F. Bo, Preparation of HA/chitosan composite coatings on alkali treated titanium surfaces through sol-gel techniques, *Mater. Lett.* 61 (18) (2007) 3970–3973.
- [37] T.L.E. Van Westering, C.A. Betts, M.J.A. Wood, Current understanding of molecular pathology and treatment of cardiomyopathy in duchenne muscular dystrophy, *Molecules* 20 (5) (2015) 8823–8855.

- [38] Y.-K. Wang, X. Yu, D.M. Cohen, M.A. Wozniak, M.T. Yang, L. Gao, J. Eyckmans, C. S. Chen, Bone morphogenetic protein-2-induced signaling and osteogenesis is regulated by cell shape, RhoA/ROCK, and cytoskeletal tension, *Stem Cell. Dev.* 21 (7) (2012) 1176–1186.
- [39] J. Kim, H.D. Kim, J. Park, E.-s. Lee, E. Kim, S.S. Lee, J.-K. Yang, Y.-S. Lee, N. S. Hwang, Enhanced osteogenic commitment of murine mesenchymal stem cells on graphene oxide substrate, *Biomater. Res.* 22 (1) (2018) 1–9.
- [40] F. Ciobanu, M. Golzio, E. Kovacs, J. Teissié, Control by low levels of calcium of mammalian cell membrane electropermeabilization, *J. Membr. Biol.* 251 (2) (2018) 221–228.
- [41] R.J. Waddington, R. Moseley, G. Embery, Reactive oxygen species: a potential role in the pathogenesis of periodontal diseases, *Oral Dis* 6 (3) (2000) 138–151.
- [42] A. Mantovani, A. Sica, M. Locati, Macrophage polarization comes of age, *Immunity* 23 (4) (2005) 344–346.
- [43] J. Li, X. Jiang, H. Li, M. Gelinsky, Z. Gu, Tailoring materials for modulation of macrophage fate, *Adv. Mater.* 33 (12) (2021), e2004172.
- [44] X.Y. Fang, Y.X. Zhan, X.M. Zhou, L.N. Wu, J. Lin, Y.T. Yi, C.M. Jiang, J. Wang, J. Liu, CXCL12/CXCR4 mediates orthodontic root resorption via regulating the M1/M2 ratio, *J. Dent. Res.* (2021), <https://doi.org/10.1177/00220345211050324>.
- [45] Y. Zhu, H. Liang, X. Liu, J. Wu, C. Yang, T.M. Wong, K.Y.H. Kwan, K.M.C. Cheung, S. Wu, K.W.K. Yeung, Regulation of macrophage polarization through surface topography design to facilitate implant-to-bone osteointegration, *Sci. Adv.* 7 (14) (2021).
- [46] B. Kelly, L.A. O'Neill, Metabolic reprogramming in macrophages and dendritic cells in innate immunity, *Cell Res* 25 (7) (2015) 771–784.
- [47] E. Rendra, V. Riabov, D.M. Mossel, T. Sevastyanova, M.C. Harmsen, J. Kzhyshkowska, Reactive oxygen species (ROS) in macrophage activation and function in diabetes, *Immunobiology* 224 (2) (2019) 242–253.
- [48] T. Wang, H. Liu, G. Lian, S.Y. Zhang, X. Wang, C. Jiang, HIF1 $\alpha$ -Induced glycolysis metabolism is essential to the activation of inflammatory macrophages, *Mediat. Inflamm.* 2017 (2017) 9029327.
- [49] R.H. Deng, M.Z. Zou, D. Zheng, S.Y. Peng, W. Liu, X.F. Bai, H.S. Chen, Y. Sun, P. H. Zhou, X.Z. Zhang, Nanoparticles from cuttlefish ink inhibit tumor growth by synergizing immunotherapy and photothermal therapy, *ACS Nano* 13 (8) (2019) 8618–8629.
- [50] J.L. Wang, K.F. Ren, H. Chang, F. Jia, B.C. Li, Y. Ji, J. Ji, Direct adhesion of endothelial cells to bioinspired poly(dopamine) coating through endogenous fibronectin and integrin  $\alpha 5 \beta 1$ , *Macromol. Biosci.* 13 (4) (2013) 483–493.
- [51] P. Friedl, B. Weigelin, Interstitial leukocyte migration and immune function, *Nat. Immunol.* 9 (9) (2008) 960–969.
- [52] L. Lv, Y. Xie, K. Li, T. Hu, X. Lu, Y. Cao, X. Zheng, Unveiling the mechanism of surface hydrophilicity-modulated macrophage polarization, *Adv. Healthcare Mater.* 7 (19) (2018), e1800675.
- [53] F.Y. McWhorter, C.T. Davis, W.F. Liu, Physical and mechanical regulation of macrophage phenotype and function, *Cell. Mol. Life Sci.* 72 (7) (2015) 1303–1316.
- [54] L. Yu, Y. Hou, W. Xie, J.L.C. Camacho, C. Cheng, A. Holle, J. Young, B. Trappmann, W. Zhao, M.F. Melzig, E.A. Cavalcanti-Adam, C. Zhao, J.P. Spatz, Q. Wei, R. Haag, Ligand diffusion enables force-independent cell adhesion via activating  $\alpha 5 \beta 1$  integrin and initiating rac and RhoA signaling, *Adv. Mater.* 32 (29) (2020), e2002566.
- [55] A. Hall, Rho GTPases and the actin cytoskeleton, *Science* 279 (5350) (1998) 509–514.
- [56] Y. Xu, K. Cui, J. Li, X. Tang, J. Lin, X. Lu, R. Huang, B. Yang, Y. Shi, D. Ye, J. Huang, S. Yu, X. Liang, Melatonin attenuates choroidal neovascularization by regulating macrophage/microglia polarization via inhibition of RhoA/ROCK signaling pathway, *J. Pineal Res.* 69 (1) (2020), e12660.
- [57] J. Xu, J. Yang, A. Nyga, M. Ehteramy, A. Moraga, Y. Wu, L. Zeng, M.M. Knight, J. C. Shelton, Cobalt (II) ions and nanoparticles induce macrophage retention by ROS-mediated down-regulation of RhoA expression, *Acta Biomater* 72 (2018) 434–446.
- [58] J. Kim, H.Y. Kim, S.Y. Song, S.H. Go, H.S. Sohn, S. Baik, M. Soh, K. Kim, D. Kim, H. C. Kim, N. Lee, B.S. Kim, T. Hyeon, Synergistic oxygen generation and reactive oxygen species scavenging by manganese ferrite/ceria Co-decorated nanoparticles for rheumatoid arthritis treatment, *ACS Nano* 13 (3) (2019) 3206–3217.